*J Mater Sci* (2023) 58:11139–11158

Electronic materials

# Morphology of highly stable lead-free hybrid organic–inorganic double perovskites $(CH_3NH_3)_2XBiCl_6$ (X = K, Na, Ag) for solar cell applications

Neelu Neelu[1], Nivedita Pandey[1], and Subhananda Chakrabarti[1,*]

[1] *Department of Electrical Engineering, Indian Institute of Technology Bombay, Mumbai 400076, India*

**Received:** 11 March 2023
**Accepted:** 16 June 2023
**Published online:** 5 July 2023



## ABSTRACT

The power conversion efficiency (PCE) of single structured perovskite solar cells (PSCs) has achieved a remarkable value of 25.2% over the last ten years. But these PSCs are not eco-friendly and suffer from the serious issue of stability. So it is very important to investigate greener and more stable alternatives to these perovskite materials. In recent years, lead-free double perovskite (DP) materials have surfaced as an ecologically favorable photovoltaic material due to their inherent chemical stability, modest carrier effective masses, suitable bandgaps, and low exciton binding energies. Herein, we have synthesized lead-free, highly stable, good quality, cheaper and environment friendly halide-based hybrid organic–inorganic double perovskite $(MA)_2XBiCl_6$ (MA = $CH_3NH_3$, X = K, Na, Ag) by adopting one step hydrothermal route having the morphology of vertical flakes and micro-rods. Further, we have analyzed the morphological, photo-physical, chemical, electronic, and structural behavior of synthesized samples by using various characterization techniques. We elucidated the formation of high-quality, stable, and highly crystalline luminescent DP nanoparticles (NPs). Moreover, we fabricated three solar cell devices using the three as-synthesized DPs and further demonstrated that the solar cell device using $MA_2NaBiCl_6$ NPs as absorber layer have 2.09% PCE performed better as compared to $MA_2KBiCl_6$ and $MA_2AgBiCl_6$ based devices. Our work reports a first lead-free double perovskite solar cell with different three-dimensional morphology shedding light on the shape manipulation and providing a feasible alternative to toxicity issues in single perovskite and further encouraging rigorous research on these materials for future photovoltaic technology.

Handling Editor: David Cann.

Address correspondence to E-mail: subho@ee.iitb.ac.in
E-mail Addresses: sharmaneelu627@gmail.com; niveditapandey.iitb@gmail.com

https://doi.org/10.1007/s10853-023-08704-z

## Introduction

The constant rise in global energy consumption has promoted the development of PV technology. In this community, perovskite-based solar cells have been considered a leading PV material because Lead halide-based single perovskites have recently earned a lot of interest due to their adjustable direct bandgaps, balanced electron and hole effective masses, high optical absorption coefficient, defect tolerance, small exciton binding energies, and super-long photo-generated carrier diffusion lengths and lifetimes [1–15]. Depending on the A-site cation, halide-based single celled perovskites with the generic formula $ABX_3$ (A: $CH_3NH_3^+$, $Cs^+$; B: $Sn^{2+}$, $Pb^{2+}$; X: $Cl^-$, $I^-$, $Br^-$) can be split into two categories: One is inorganic halide perovskite having A as an inorganic element and other is organic–inorganic hybrid halide perovskite having A as organic compound. The first PSCs in photovoltaics is reported by A. Kojima in 2009 based on organic–inorganic hybrid halide perovskites Methyl ammonium lead iodide ($MAPbI_3$, -MA is $CH_3NH_3^+$) and Methyl ammonium lead bromide ($MAPbBr_3$) to replace the sensitizer in the liquid dye-sensitized-based solar cells (DSSC) with the PCE of 3.8% [16]. These PSCs did not attract significant attention due to quite a low efficiency and poor stability. At the laboratory scale, the recorded PCE of solar cells based on these perovskite materials has improved significantly from 3.8 to 29.8% from 2009 to 2023 [16–33]. In addition to solar cells, these perovskite materials have been used in various optoelectronic applications, like lasers, light-emitting diodes (LEDs), X-ray detectors, and photodetectors [34–39]. Along with the various advantages of the lead-based perovskites, there are two major concerns associated with them, first is the toxicity nature of lead, and the second is the long-term stability issue in the presence of moisture, light and heat, which can further stymie the development of lead halide perovskite-based photovoltaic and optical devices [39]. In this regard, substantial research has been done to find non or low-toxic, air-stable perovskite-based materials [40–45]. Significant critical efforts have been done in recent decades to explain the underlying origins of Lead halide perovskite's exceptional and unique photovoltaic characteristics. The remarkable symmetry of the perovskite structure, as well as the specific electronic arrangement of Lead ($6s^2$ $6p^0$), have played a major role in influencing the optoelectronic capabilities of lead halide perovskites [43, 44]. In this respect, analogous divalent lone-pair metal cations like Sn (II) and Ge (II) could be a possible substitute for Pb(II). But at the other hand, Sn (II) and Ge (II)-based halide perovskites, have more significant instability problems against the oxidation state because Sn (II) and Ge (II) can be easily converted into Sn (IV) and Ge (IV) in ambient temperature due to the exceptionally high-energy of Sn (II) $5s^2$ and Ge (II) $4s^2$ states, and also due to their small ionic radii [46]. Moreover, trivalent cations like Bi (III) and Sb (III) have been used in place of divalent Pb(II) but the resultant structures cannot maintain the charge neutrality with the chemical formula $A_3B_2X_9$ which further leads to unwanted photovoltaic features such as huge anisotropic carrier effective masses, high bandgaps and low defect tolerance behavior [47, 48].

The concept of maintaining high electronic dimensionality in the framework of structural dimensionality is vital to consider while looking for Lead-free halide perovskites as promising and a potential candidate for solar cell absorbers [40]. Therefore maintenance of the three-dimensional (3D) structure with the replacement of Lead could be the most favorable strategy that can be achieved by cation transfiguration in lieu of replacing the two divalent $Pb^{2+}$ cations with two different cations, one is a monovalent cation and another is a trivalent cation which further leads to a 3D double perovskite structure with formula $A_2B(I)B(III)X_6$ which further allow the additional flexibility in selecting B-cation elements [49, 50]. In addition to the double perovskites materials, Cs-based lead-free halide quadruple perovskites materials ($Cs_4MnBi_2Cl_{12}$, $Cs_4CdBi_2Cl_{12}$, $Cs_4MnSb_2Cl_{12}$, and $Cs_4CdSb_2Cl_{12}$) are also reported having 3D structure which have been synthesized and found to be highly crystalline, along with long carrier lifetime, and low trap-state densities [51]. To date, few double perovskites have been synthesized having monovalent cation B(I) as $Ag^+$, $Li^+$, $Rb^+$, $Na^+$, $K^+$, and $Ti^+$ and trivalent cation B(III) as $Sb^{3+}$, $Ga^{3+}$, $Al^{3+}$, $Tl^{3+}$, $In^{3+}$, $Bi^{3+}$, and some other lanthanides and a trivalent transition metal. These halide-based lead-free double perovskites have gained a lot of attention as attractive optoelectronic prospects because of their cubic structure (Fm3m) that allows them to extend in all three dimensions with corner-sharing metal halide octahedra having

application in various domains including X-ray photodetectors, photocatalyst, electrocatalyst, solar cells, and LEDs. But, among these proposed double perovskite materials, very few of them have been experimentally realized in the laboratory for the development of solar cell having significant poer conversion efficiency [52–55].

The quest for lead-free and low-cost photovoltaics has encouraged researchers to investigate organic materials having conducting and semiconducting properties for their possible alternatives [56]. The advantages of the organic materials investigated by past researchers over the years is having low manufacturing cost, and high absorption coefficient which leads to significant impact on organic photovoltaic solar cell [57, 58]. Leveraging all these benefits and current considerable improvements in power conversion efficiency (PCE) has resulted in the creation of several initial commercial organic photovoltaic (OPV) devices. To further enhance the efficiency of photovoltaic (PV) devices, researcher has found Organic–inorganic hybrid solar cells combination is having advantages of both organic as well as inorganic material [59]. The advantages associated with the addition of inorganic material to organic material is to reduce the photo induced degradation of the organic photovoltaic devices in addition to increase in the charge carriers photo generation through the absorbed exciton in the inorganic material [60]. Moreover, inorganic materials have high light absorption in comparison with the organic materials [61, 62]. These interesting properties encourages us to build a hybrid organic–inorganic lead-free solar cell in replacement of the lead-based halide perovskites solar cell.

Here in this study, we report the first solar cell devices based on double perovskite nanomaterials $MA_2XBiCl_6$ (X = K, Na, Ag). Firstly we have synthesized MA-based non-toxic and non-degradable halide double perovskite $MA_2XBiCl_6$ (X = K, Na, Ag) using a simple one-step hydrothermal synthesis technique. Further, we have characterized these three synthesized materials to investigate the phase, optical behavior, chemical nature, surface morphology, absorption nature, and band gap. The obtained characterization results of all these three materials suggest them as promising and stable absorber candidates and solar cells based on these materials showed remarkable PCE having the highest value for $MA_2NaBiCl_6$ NPs. Our present study provides the access to the high-quality and large-scale fabrication of solar cell devices and throws light on further investigation of morphologically tuned non-toxic and cheaper DP materials for a wide range of applications with very high and stable performance in the photovoltaics domain.

## Details of experiments

### Chemicals used

The chemicals which were used in the synthesis process of material were purchased from Sigma Aldrich and have we utilized these materials in their original configuration without any additional treatment. Methyl ammonium (MA) solution, Potassium chloride (KCl, 99%), Silver chloride (AgCl, 99%), Sodium chloride (NaCl, 99%), Bismuth chloride ($BiCl_3$, 99%), Acetone (≥ 99.9%), Hydrochloric acid (HCl), and Ethyl acetate (≥ 95%) were utilized into our synthesis method.

### Synthesis process details

#### *Preparation of methylammonium chloride (MACl) solution*

Initially, we synthesized MACl solution by taking the equimolar amount of MA solution in HCl at room temperature and then heated the solution mixture at 50 °C till the solution is completely dry. Further, we cleaned the obtained product with acetone to remove the unwanted byproducts and then dried it for 24 h in an oven. The prepared MACl was used to synthesize the three double perovskites, i.e., $MA_2XBiCl_6$ (X is K, Na, Ag) by one-step hydrothermal process.

#### *Preparation of $MA_2KBiX_6$ NPs, X is K, Na, Ag*

The $MA_2KBiCl_6$ NPs were synthesized by adopting a one-step hydrothermal method after taking MACl, KCl, and $BiCl_3$ precursors in 2, 1, and 1 molar ratios, respectively, in the 1 ml HCl solution kept in a stainless steel autoclave. Then, the complete solution was heated at 160 °C for 8 h to perform the high-pressure reaction. Further, the temperature was cooled down to room temperature and the obtained product was filtered and cleaned using the solvent

precipitation technique to remove the byproducts. Finally, the cleaned product was heated at 60 °C in a vacuum oven to dryness.

## Characterization details

The X-ray diffraction (XRD) experiment was performed by X-ray powder diffractometer with the Copper (Cu) $K_\alpha$ radiation having wavelength of 1.54 Å at the voltage and current of 40 kV and 30 mA value respectively, with variation of the angle (2θ) values (10° to 50°) with peak intensity (arbitrary unit) at an increment of 0.1° to investigate the quality, and to confirm the crystalline phases and purity of the synthesized DP materials. The sample for XRD measurement was prepared by drop casting a concentrated NP solution on the substrate and the diffraction peaks were observed using symmetric reflection mode and parallel beam geometry at room temperature. Further, the obtained results were analyzed using PANalytical Xpert HighScore 4.1 software. The optical property of the synthesized DP NPs was examined by doing room temperature Photoluminescence (PL) measurement which is a type of electromagnetic (EM) spectroscopy that evaluates the fluorescent compounds. The measurements were performed using PL Fluorolog-3 Spectroscopy with the help of a Light Source of 450 W Xenon Lamp having a scanning speed of 150 nm/sec, wavelength accuracy of 0.5 nm, and wavelength range of 200 nm to 700 nm. In the PL setup, a 300 nm continuous-wave laser source having an incidence intensity of 100 mW/cm$^2$ with two monochromators (visible and near-infrared (NIR)) connected in series was used for the excitation purpose. The above setup can quickly and accurately determine the presence of molecular elements in the sample by utilizing the phenomena of electronic excitation caused by the interaction of high-energy particles (HEPs) such as excited electrons and photons with electrons. Using a Shimadzu ultraviolet–visible (UV–vis) absorption spectrometer having range of wavelength 200–800 nm, a resolution of 0.05 nm, slit width of 2 nm, and scan interval of 1 nm, UV–vis spectroscopy of the as-synthesized NPs was collected to examine the absorbance phenomena. Field emission gun-scanning electron microscopy (FEG-SEM) has been used to reveal the structural morphology using the JEOL JSM-7600F model with a secondary electron image (SEI) resolution of 1.0 nm at 15 kV with accelerating voltage varying from 0.1 to 30 kV at low & high magnification of 25 X and 1,000,000 X, respectively. A Schottky field emission gun and an electron column with semi-in-lens detectors were employed in the JEOL JSM-7600F to deliver ultra-high-resolution with a variety of probe currents (1pA to more than 200 nA). In addition, the chemical composition and presence of functional groups in the synthesized DPs are analyzed by using Fourier Transform Infrared (FTIR) spectroscopy done using the Spectrum 100 FT-IR system of PerkinElmer.

## Device fabrication detail

A simple solar cell has been fabricated with all the three as-synthesized DP as absorbing layer. Fluorine doped tin oxide (FTO) on transparent glass (7 Ω per square) substrate on which contact deposition of Gold (Au) has been used to fabricate the device. We have extensively cleaned substrate by deionized (DI) water, ethanol, and acetone by performing ultrasonication for 45 min and further ultraviolet (UV)-ozone for 20 min treatment has been applied. $SnO_2$ of FTO substrate is working as electron transport layer. $SnO_2$ layer is came out by the fluorine doped tin oxide (FTO) coated transparent glass substrate which is modified by the oxygen plasma assisted reaction for 12 min at room temperature to form the pure $SnO_2$ phase. Then obtained uniform solution of as-synthesized DPs materials $MA_2XBiCl_6$ (X is K, Na, Ag) was uniformly coated using spin-coating on the substrate at 900 rotation per minute (rpm) for 15 s and 2000 rpm for 20 s, respectively. The above process was repeated many times for obtaining a uniformity of absorber layer coated on substrate. Afterward, the DP-coated FTO substrate was annealed at 250 °C for 10 min and then allowed to ramp down to the temperature of 30 °C. Finally, 100 nm thick Au contacts were deposited with a deposition rate of 0.5 nm/sec and a chamber pressure of $2.5 \times 10^{-6}$ mbar using a mask in a 6-target Electron beam evaporation system. The *I–V* characteristics of fabricated solar cell devices were measured in dark and light by utilizing an in-house solar simulator. Also, the Bentham PVE300 system was used to calculate the external quantum efficiency (EQE) of the fabricated devices using a Xenon lamp source with Si and Ge detectors having a wavelength range from 300 to 1800 nm with a resolution of 2 nm.

## Results and discussions

The schematic 3D crystal structure of double perovskite materials $MA_2XBiCl_6$ (X = K, Na, Ag) formed by alternatively positioned KCl6 (NaCl6 or AgCl6) and BiCl6 octahedra resulting in a doubly celled perovskite as compare to its single perovskite counterpart is shown in Fig. 1a. In this crystal structure, the B site is occupied by the Potassium (K)/Sodium (Na)/Silver (Ag), and B′ site is occupied by the Bi (Bismuth) element. The structural investigation of synthesized DPs $MA_2XBiCl_6$ (X is K, Na, Ag) NPs was done using the room temperature XRD technique. The XRD pattern was observed in order to examine the phases and purity of the synthesized materials. Figure 1b–d represent the XRD pattern of $MA_2KBiCl_6$, $MA_2NaBiCl_6$, and $MA_2AgBiCl_6$ DP, respectively, revealing that newly synthesized MA-based halide DPs NPs form a rhombohedral $R\bar{3}m$ space group [63]. The peaks shown in the XRD pattern of all three materials have good accord with the standard reported data with well-indexing and also, demonstrates that the newly described synthesis process yields high-quality, and crystalline double perovskite materials [63–66]. The additional peak (marked *) in the XRD pattern of $MA_2KBiCl_6$ DPs around 34 ° is due to the precursors utilized in the synthesis process of the material. The diffraction peaks are indexed as (111), (022), (113), (222), (004), (024), (224), (044), and (244) planes of the crystal structure for materials $MA_2XBiCl_6$ (X = K, Na, Ag) showing the absence of any secondary phase diffraction peaks.

Furthermore, from the XRD data, we have calculated the full-width half maxima (FWHM), and crystallite size as given in Table 1 using Scherrer's equation [64]:

$$D = \frac{K\lambda}{\beta \cos\theta} \tag{1}$$

$$\beta = \frac{1}{2}(2\theta_{max} - 2\theta_{min}) \tag{2}$$

where $D$ is crystallite size, $\lambda$ is the wavelength of X-rays used in XRD characterization of samples, $K$ is

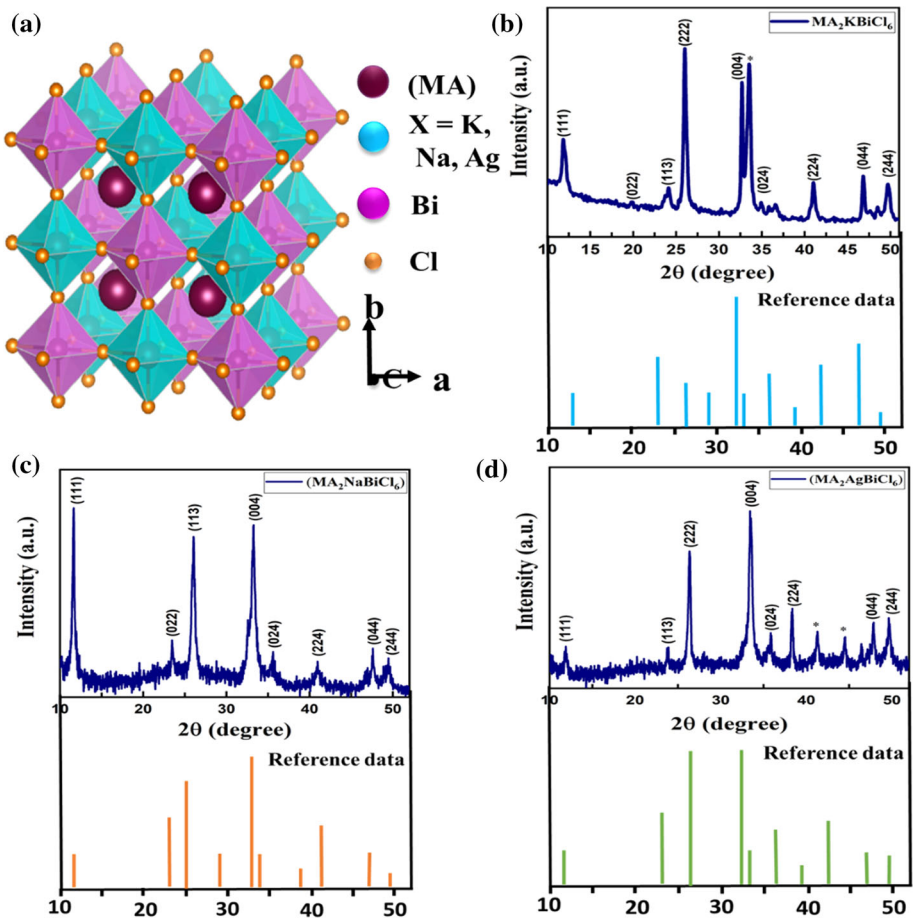


**Figure 1** **a** Schematic representation of crystal structure geometry of $MA_2XBiCl_6$ (X = K, Na, Ag) having $KCl_6$ ($NaCl_6$ or $AgCl_6$) and $BiCl_6$ octahedra and XRD pattern of the synthesized double perovskite nanoparticles **b** $MA_2KBiCl_6$ **c** $MA_2NaBiCl_6$ and **d** $MA_2AgBiCl_6$ with their respective standard.

**Table 1** Full width half maxima and crystallite size calculated from XRD data by utilizing Scherrer's equation

| S. no | Materials name | $2\theta$ at $I_{max}$ | $2\theta_{max}$ | $2\theta_{min}$ | FWHM | Cos $\theta$ | $D$ (nm) |
|---|---|---|---|---|---|---|---|
| 1 | $MA_2KBiCl_6$ | 26° | 25° | 27° | 0.0174 | 0.974 | 8.12 |
| 2 | $MA_2NaBiCl_6$ | 33° | 31° | 34° | 0.0261 | 0.958 | 5.54 |
| 3 | $MA_2AgBiCl_6$ | 33° | 32° | 34° | 0.0174 | 0.958 | 8.31 |

**Table 2** Lattice constant (a, c) and interplanar distance (d) of all the synthesized double perovskite nanomaterials

| S. no | Materials name | (a, c) | d (pm) | | | | | | | | |
|---|---|---|---|---|---|---|---|---|---|---|---|
| | | (Å) | (111) | (022) | (113) | (222) | (004) | (024) | (224) | (044) | (244) |
| 1 | $MA_2KBiCl_6$ | 7.84, 20.99 | 452 | 277 | 236 | 226 | 195 | 175 | 159 | 138 | 130 |
| 2 | $MA_2NaBiCl_6$ | 7.37, 20.47 | 425 | 260 | 222 | 212 | 184 | 164 | 150 | 130 | 122 |
| 3 | $MA_2AgBiCl_6$ | 6.81, 19.21 | 392 | 240 | 205 | 196 | 170 | 152 | 138 | 120 | 113 |

Scherrer's constant, β is the full width at half maximum, $\theta$ is the peak position, and $2\theta_{max}$ and $2\theta_{min}$ is the right and left side 2θ value where intensity is half of the maximum at that peak [64] calculated from XRD plots. For calculation of FWHM, we have taken $K = 0.9$, and $\lambda = 0.154$ nm as used in the XRD experiment.

In addition, we have calculated the lattice constants (a, c) using Brag's diffraction law and interplanar distance (d) for all the three synthesized double perovskite nanomaterials using the below formula [65], and the calculated values for all the planes are summarized in Table 2.

$$2d \sin\theta = n\lambda \tag{3}$$

$$\frac{1}{d_{hkl}^2} = \frac{h^2 + k^2}{a^2} + \frac{l^2}{c^2} \tag{4}$$

where $\theta$ is the angle, n is the order of diffraction, $\lambda$ is the wavelength of X-rays, and ($h$ $k$ $l$) is the corresponding plane.

To know the structural stability of all the three synthesized DPs, we calculated the tolerance factor (t) and octahedral factor ($\mu$) summarized in Table 3. The obtained values are in the standard range required to form a stable double perovskite structure. The tolerance and octahedral factor are calculated by utilizing the below equations [66]:

$$t = 0.71 \frac{R_A + R_X}{R_{avg} + R_X} \tag{5}$$

$$\mu = \frac{R_{avg}}{R_X} \tag{6}$$

Here, $R_A$ & $R_X$ is the ionic radii of cation A (MA) and halide X (Cl, Br, I); respectively, $R_{avg}$ is the average ionic radii of B′ and B″ ion [67–70].

The FEG-SEM images were recorded to know the surface morphology and crystallinity of the synthesized double perovskite materials. Figure 2a–c shows FEG-SEM image of $MA_2KBiCl_6$, $MA_2NaBiCl_6$ and $MA_2AgBiCl_6$ DP NPs, respectively, at 1 µm scale of resolution. The morphology of $MA_2KBiCl_6$ was observed to be dense, and homogeneous with vertically aligned flakes structure with pure crystallinity throughout the area as shown in Fig. 2a. The microrod type surface morphology for $MA_2NaBiCl_6$ and $MA_2AgBiCl_6$ DP NPs was observed from the FEG-SEM images having length and diameter of 0.17 µm and 1.90 µm, respectively. The observed FEG-SEM images confirm the formation of excellent nanostructures as compared to the previously reported work on double perovskite nanostructures with a variation in the morphology from nanoflakes to nanorod [64]. Also, our group is reporting a rod-like microcrystal structure in $MA_2AgBiCl_6$ DP for the first time.

To examine the optical transitions, carrier dynamics, and applicability of synthesized materials for photovoltaic application, we performed the photoluminescence experiment at room temperature with a 300 nm fixed excitation wavelength and calculated their optical band gap. Figure 3a–c indicates the PL profile of $MA_2KBiCl_6$, $MA_2NaBiCl_6$, and $MA_2AgBiCl_6$, respectively, at 300 K. The PL spectra of $MA_2KBiCl_6$ DP indicate a sharp and luminescent peak at the wavelength of 320 nm corresponding to

**Table 3** Tolerance Factor and octahedral factor of the synthesized double perovskite materials

| S. no | Name of the material | Tolerance factor ($t$) | Octahedral factor (μ) |
|---|---|---|---|
| 1 | $MA_2KBiCl_6$ | 0.93 | 0.66 |
| 2 | $MA_2NaBiCl_6$ | 0.98 | 0.56 |
| 3 | $MA_2AgBiCl_6$ | 0.97 | 0.59 |

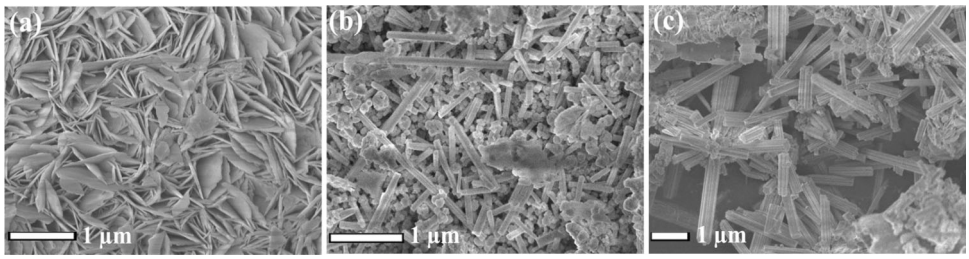


**Figure 2** FEG-SEM image of synthesized double perovskite nanoparticles at a 1 μm resolution scale for **a** $MA_2KBiCl_6$ **b** $MA_2NaBiCl_6$ and **c** $MA_2AgBiCl_6$.

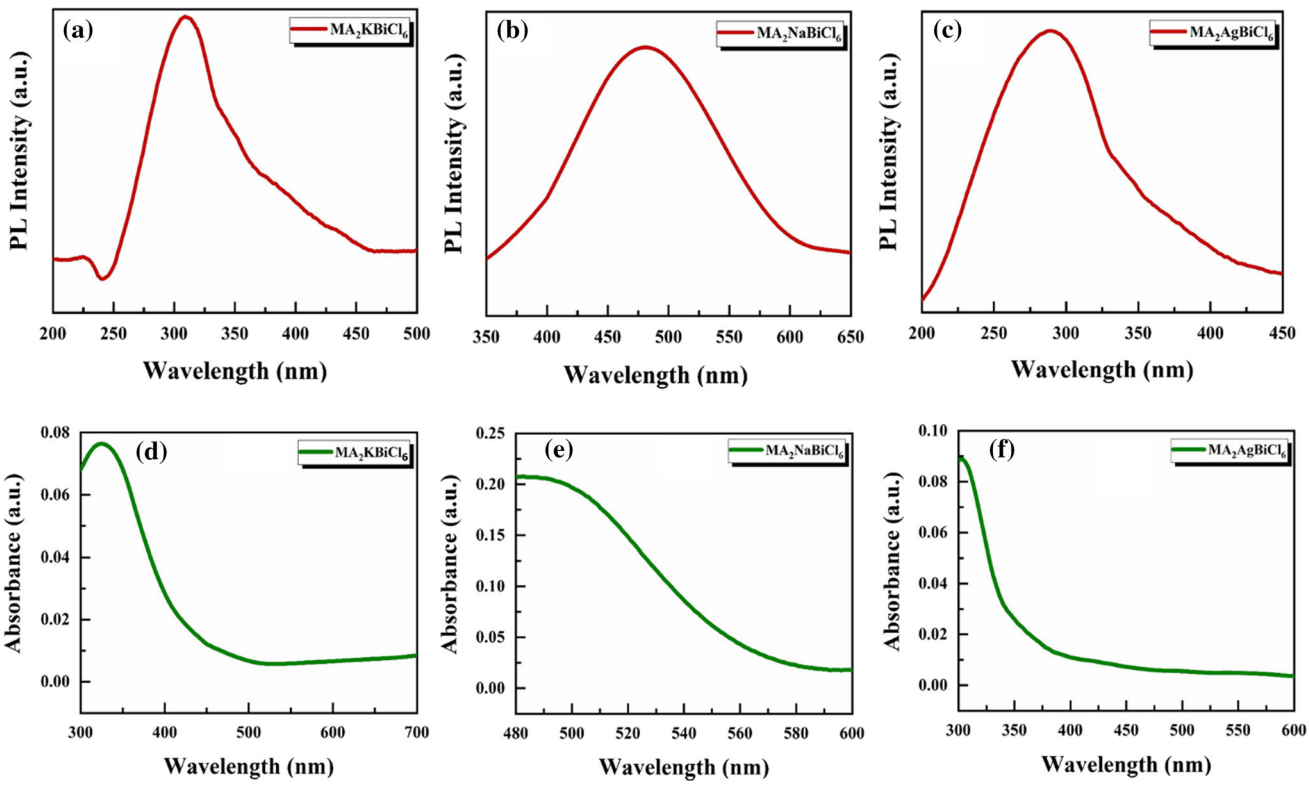


**Figure 3** Illustrates the PL spectra of **a** $MA_2KBiCl_6$ **b** $MA_2NaBiCl_6$, and **c** $MA_2AgBiCl_6$ and absorbance profile of **d** $MA_2KBiCl_6$ **e** $MA_2NaBiCl_6$ and **f** $MA_2AgBiCl_6$ DPs.

an energy of 3.87 eV as shown in Fig. 3a. A broad PL peak at a wavelength of 480 nm (2.58 eV) and 300 nm (4.13 eV) has been observed for the $MA_2NaBiCl_6$ and $MA_2AgBiCl_6$ DP as shown in Fig. 3b, c, respectively. PL emission peaks of all three synthesized double perovskite material is comparable to the recent papers on related halide perovskites [71–74]. Also, the absorption profile of the as-synthesized double perovskite materials was determined by UV–VIS absorption spectrometer in 200–800 nm of the wavelength range. Figure 3d–f represent the absorption profile of $MA_2KBiCl_6$, $MA_2NaBiCl_6$, and

$MA_2AgBiCl_6$, respectively, at 300 K. From the absorption profile of all three material, a very good absorption behavior has been observed for the synthesized materials. The absorption peak rises at 465 nm (2.66 eV), 564 nm (2.19 eV), and 386 nm (3.21 eV with a sharp peak at 325 nm (3.81 eV), 482 nm (2.57 eV) and 325 nm (3.90 eV) for $MA_2KBiCl_6$, $MA_2NaBiCl_6$ and $MA_2AgBiCl_6$ as shown in Fig. 3d–f, respectively.

Further, from the optical absorption spectra, we have evaluated the band gap of synthesized double perovskite materials using the Tauc plot and these materials are showing an indirect band gap behavior which are in agreement with the previously reported results on similar type of materials [64, 75–80]. A Tauc plot of $(\alpha h\vartheta)^{0.5}$ verses wavelength indicate the material's indirect band gap nature as shown in Fig. 4a–c for synthesized DP $MA_2KBiCl_6$, $MA_2NaBiCl_6$ and $MA_2AgBiCl_6$, respectively. Here $\alpha$ and $h\vartheta$ represent the material's absorption coefficient and energy of photons, respectively. The calculated indirect band gap are 2.51 eV, 2.06 eV, and 2.80 eV for $MA_2KBiCl_6$, $MA_2NaBiCl_6$ and $MA_2AgBiCl_6$, respectively. In the reference [64], the reported band gap of $MA_2KBiCl_6$ is 3.37 eV and 3.04 eV but our evaluated indirect band gap is 2.51 eV. The reason behind the difference in results could be change of material's phase to achieve stability leading to a change in band gap value [75, 81]. The materials is showing low band gap which clearly indicating that the materials are useful in the photovoltaic applications. Two distinct phenomena are responsible for the calculation of direct and indirect band gaps as Phonon-assisted recombination and absorption mechanisms create considerable coupling effects of carrier phonon in the indirect bandgap of all double perovskite materials which results in the dark self-trapped exciton state (STE) emission condition at room temperature whereas radiative STE has been formed by an insufficient exciton-phonon coupling power in the direct bandgap [82–84].

To check the stability of all the synthesized material in the exposure to light at room temperature, we have recorded the absorption profile, PL profile and XRD profile of all the materials after 14 and 28 days. Figure 5a–c demonstrate the absorption spectra of $MA_2KBiCl_6$, $MA_2NaBiCl_6$, and $MA_2AgBiCl_6$, respectively, for freshly synthesized samples, after 14 days of synthesis and after 28 days of synthesis. It can be clearly seen from Fig. 5 that no remarkable change in absorption spectra has been observed for the synthesized material even after one month of exposure to light which further demonstrates the non-degradable and stable nature of synthesized double perovskites as compared to their single perovskite counterpart.

PL profile of the $MA_2KBiCl_6$, $MA_2NaBiCl_6$, and $MA_2AgBiCl_6$ samples just after synthesis, after 14 days of synthesis and after 28 days of synthesis is demonstrated in Fig. 6a–c, respectively. The comparative PL plot clearly indicate that the material is showing similar luminescent behavior having negligible amount of change in the spectra even after one month also. In addition, we have performed the XRD of all the samples just after synthesis, after 14 days of synthesis and after 28 days of synthesis, which is demonstrated in Fig. 6d–f, respectively. The comparative XRD profile shows a negligible decrease in intensity of samples with increase in number of days

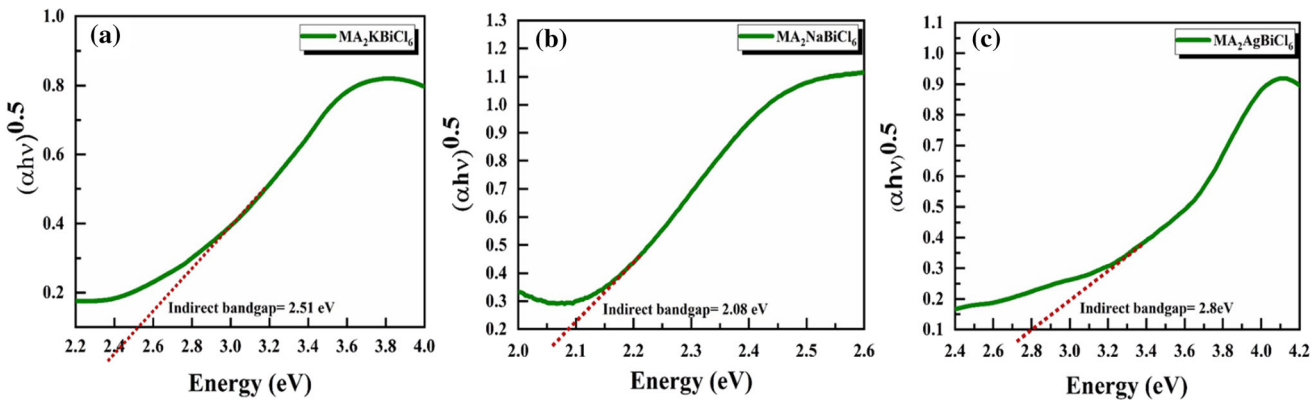


**Figure 4** Represents Tauc plot of $(\alpha h\vartheta)^{0.5}$ verses wavelength to calculate the indirect band gap of double perovskites **a** $MA_2KBiCl_6$, **b** $MA_2NaBiCl_6$, and **c** $MA_2AgBiCl_6$.

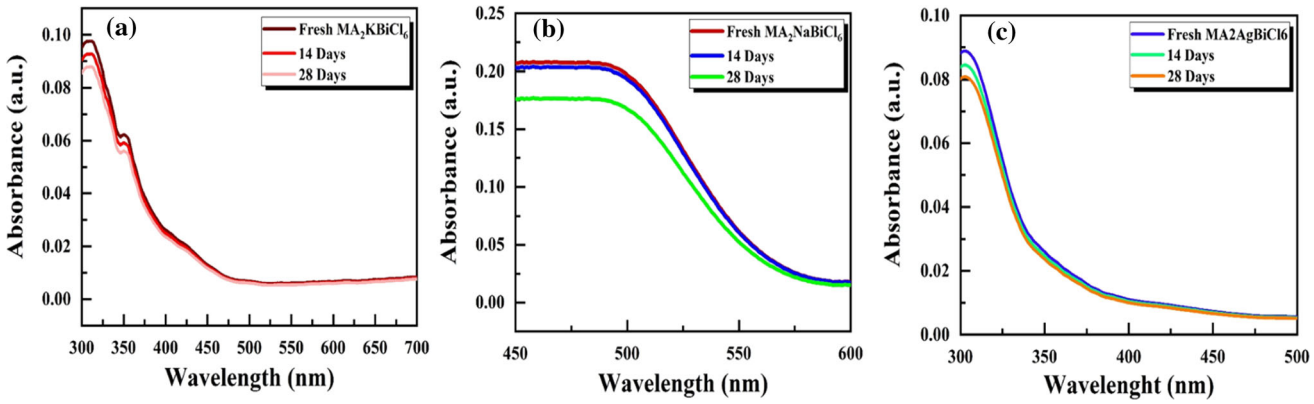


**Figure 5** Represent the absorbance spectra of **a** $MA_2KBiCl_6$ **b** $MA_2NaBiCl_6$ and **c** $MA_2AgBiCl_6$ DP after 14 and 28 days of synthesis.

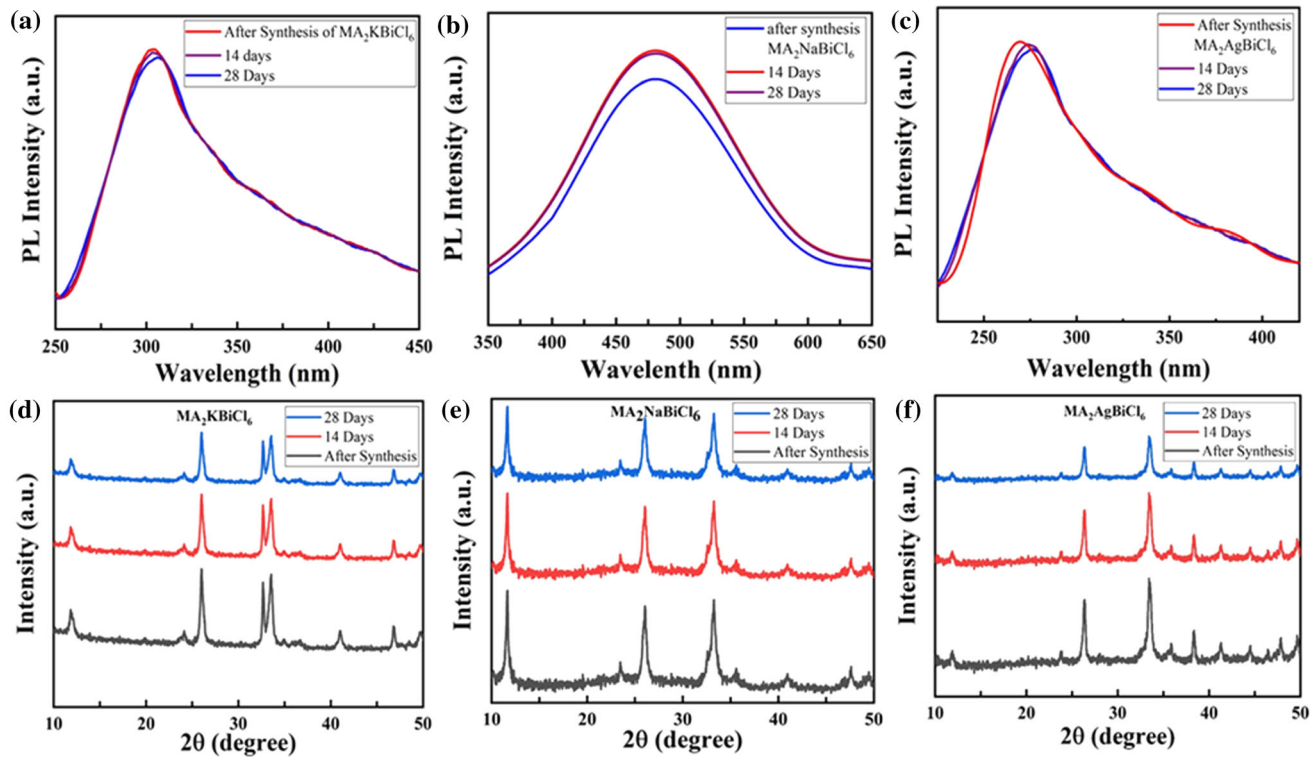


**Figure 6** Represent the PL spectra of **a** $MA_2KBiCl_6$ **b** $MA_2NaBiCl_6$ and **c** $MA_2AgBiCl_6$ DP after 14 and 28 days of synthesis and XRD spectra of **d** $MA_2KBiCl_6$ **e** $MA_2NaBiCl_6$ and **f** $MA_2AgBiCl_6$ DP after 14 and 28 days of synthesis.

which shows that the material is stable enough for photovoltaic application. Therefore, we can conclude that these synthesized DPs are showing an added advantage of having negligible degradation in the material after a month of synthesis.

FTIR spectroscopy has been done to know the presence of functional groups and other reaction by-products formed after the synthesis and cleaning of double perovskites. Figure 7a–c represent the FTIR spectra of $MA_2KBiCl_6$, $MA_2NaBiCl_6$ and $MA_2AgBiCl_6$ double perovskites materials respectively recorded at room temperature from 400 to 4000 $cm^{-1}$. In Fig. 7a, the peaks observed at 585 $cm^{-1}$, 766 $cm^{-1}$, 1296 $cm^{-1}$, and 2249 $cm^{-1}$ correspond to halogen group, C–H, alkyl metal (K), and C = C stretching bond of alkynes molecules vibrational mode respectively [85] for the synthesized $MA_2KBiCl_6$ DP. In Fig. 7b, the peaks observed at 1463 $cm^{-1}$, 1621 $cm^{-1}$, and 3523 $cm^{-1}$ correspond to the nitrosamine, diketones, and hydroxyl group

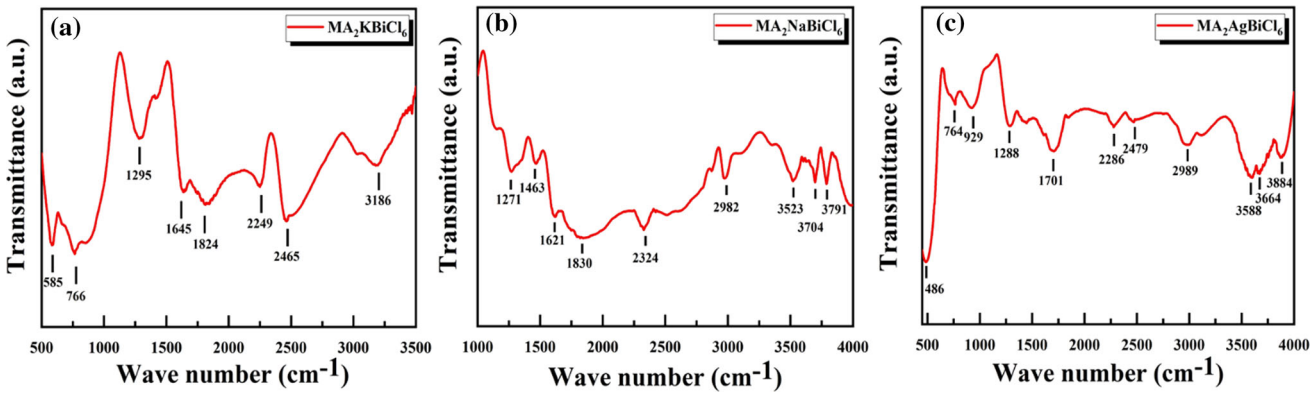


**Figure 7** FTIR profile of **a** $MA_2KBiCl_6$ **b** $MA_2NaBiCl_6$ and **c** $MA_2AgBiCl_6$ DP materials at room temperature.

vibrational mode respectively for the synthesized $MA_2NaBiCl_6$ DP. In Fig. 7c, the peak is observed at 486 $cm^{-1}$, 764 $cm^{-1}$, 1288 $cm^{-1}$, and 2989 $cm^{-1}$ corresponding to alkyl halide (AgCl), C-H group, alkyl ketones, and methyl group (MA, $CH_3NH_3$) for the synthesized DP $MA_2AgBiCl_6$. The other peaks in the FTIR spectra represent the presence of functional groups due to impurities and by-products formed during synthesis or in the cleaning of DP nanoparticles.

To test the dark current versus voltage characteristics of all the fabricated devices, we have utilized a solar simulator having −1 V to 1 V of voltage range. The dark I-V measurement utilizes electrical techniques to insert carriers into the device rather than light-generated carriers. Figure 8a–c represents the solar cell dark current verses voltage curve based on $MA_2KBiCl_6$, $MA_2NaBiCl_6$ and $MA_2AgBiCl_6$ material, respectively. Figure 8d shows the external quantum efficiency (EQE) to the wavelength curve of all three solar cell devices. EQE of all devices is almost at 20% which is quite remarkable as compared to other reported values [86]. The EQE is measured by utilizing the below equation

$$EQE = \frac{N_{\text{electrons}}}{N_{\text{photons}}} \tag{7}$$

where $N_{\text{electrons}}$ represent the flux of electrons taken from the solar cell when functioned in working conditions and $N_{\text{photons}}$ represent the flux of photons falling on the solar cell.

Further, we have fabricated three photovoltaic devices based on synthesized materials in a planar device architecture to determine the photovoltaic properties. A schematic diagram of solar cell devices with glass/FTO/DP/Au structure which is shown in Fig. 9a. To calculate the power conversion efficiency of the solar cells, we tested the light current density verses voltage characteristics of all devices. Figure 8b–d show the light current density verses voltage characteristics of solar cell with absorber layer of $MA_2KBiCl_6$, $MA_2NaBiCl_6$ and $MA_2AgBiCl_6$ DP, respectively. Moreover, the photovoltaic characteristics were evaluated from the light current density verses voltage curve. The fill factor (FF) which is an important parameter to determine the PCE can be defined as the ratio of the maximum power to the multiplication of open circuit voltage and short circuit current density. FF is calculated by the formula below [86]

$$FF = \frac{V_{MP} \times I_{MP}}{V_{OC} \times I_{SC}} \tag{8}$$

where $V_{MP}$,$I_{MP}$, $V_{OC}$, *and* $I_{SC}$ represent the voltage where power is maximum, current where power is maximum, open circuit voltage, and short circuit current, respectively, in illuminated *I–V*. Further, the PCE of all devices is calculated by utilizing the equation below [84]

$$PCE = \frac{FF \times V_{OC} \times I_{SC}}{P_{IN}} \tag{9}$$

where $P_{IN}$ is the input power of the system having the value of 0.1 W/$cm^2$. The $V_{OC}$ of solar cells based on $MA_2KBiCl_6$, $MA_2NaBiCl_6$, and $MA_2AgBiCl_6$ DP were detected from illuminated I-V characteristics which is shown in Figs. 8b, 9c, and 9d and found to be 0.90 V, 0.98 V, and 0.95 V, respectively. Further, the short circuit current density calculated from Fig. 9b–d for the solar cell devices based on

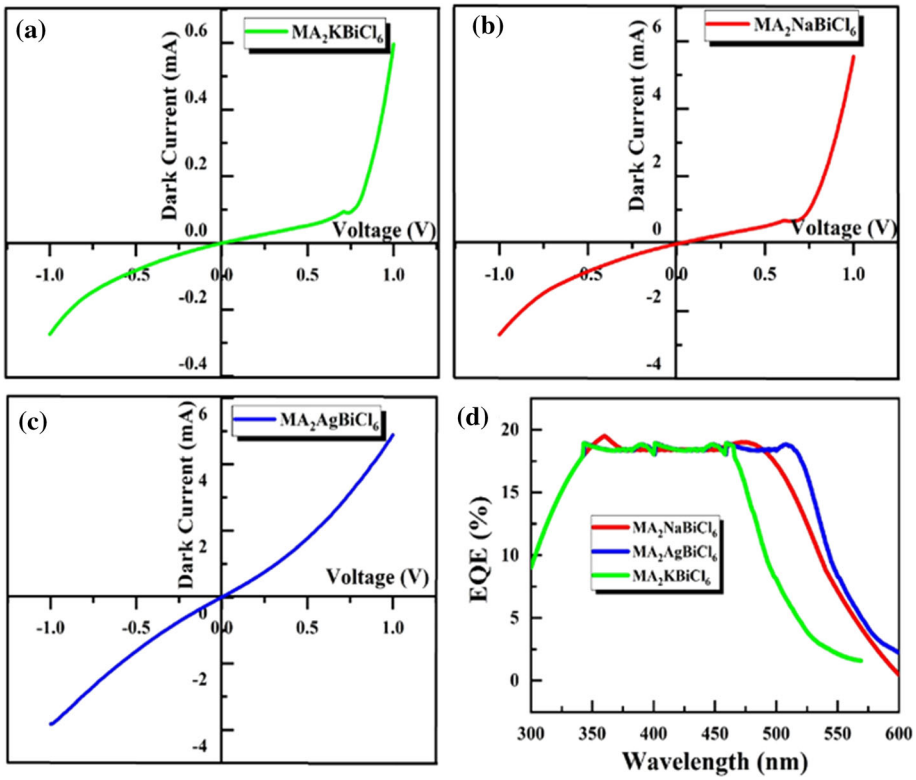


**Figure 8** Demonstrated the dark current verses voltage characteristics of **a** $MA_2KBiCl_6$, **b** $MA_2NaBiCl_6$, **c** $MA_2AgBiCl_6$, and **d** external quantum efficiency of all the synthesized DPs.

$MA_2KBiCl_6$, $MA_2NaBiCl_6$, and $MA_2AgBiCl_6$ were found to be 0.3 mA/cm$^2$, 4.0 mA/cm$^2$, and 5.0 mA/cm$^2$, respectively. From all the above-calculated parameters, the PCE of solar cell devices based on $MA_2KBiCl_6$, $MA_2NaBiCl_6$, and $MA_2AgBiCl_6$ were evaluated and found to be 0.154%, 2.09%, and 1.639%, respectively, as indicated in Fig. 9b–d. The maximum PCE of solar cell is obtained for $MA_2NaBiCl_6$ DP as compared to the other two fabricated devices indicating this material is most promising for future photovoltaic applications. The obtained photovoltaic characteristics of all the three devices that is $J_{SC}$, $V_{OC}$, FF, and PCE are given in Table 4.

Researcher are nowadays exploring the solar cell device without using either electron transport layer (ETL) or hole transport layer (HTL) and getting better performance as compared to the device with ETL and HTL [87]. This motivates us to first fabricate the device without HTL or ETL layer. We have fabricated the device having electron transport layer only but no hole transport layer. In our work SnO2 is working as electron transport layer. $SnO_2$ layer is present on FTO by the fluorine doped tin oxide (FTO) coated transparent glass substrate which is modified by the oxygen plasma assisted reaction for 12 min at room temperature to form the pure $SnO_2$ phase [88]. In this paper, the fabricated device structure is glass/FTO/$SnO_2$/DP/Au and the mechanism of transportation of the carriers is explained in details in our revised manuscript. Figure 11 shows the schematic of the energy band diagram of the fabricated device structure with $SnO_2$ as ETL and $MA_2XBiCl_6$ as absorber layer. Our as-synthesized double perovskites materials are low band gap material having good carrier mobility Which results into a good match of the alignment of the energy band between ETL and DP to separate the charge carriers [89]. When light is exposed through sun, an electron–hole pairs is generated in the absorber layer and this would go through $SnO_2$ to the FTO/Au electrode [90]. The conduction and valence band energy of FTO, ETL, DP, and Au is shown in Fig. 10. Due to the high electron mobility of $SnO_2$ and low conduction band offset, photo-generated electrons will migrate and will reach to FTO and electron current will dominate in the device. Due to low offset of valence and offset, the depletion layer will form in DP layer which lead to the fast transportation of holes. This will further help to enhance the fill factor and hence the overall device performance.

The devices based on the $MA_2NaBiCl_6$ and $MA_2AgBiCl_6$ having rod-like microcrystal structure

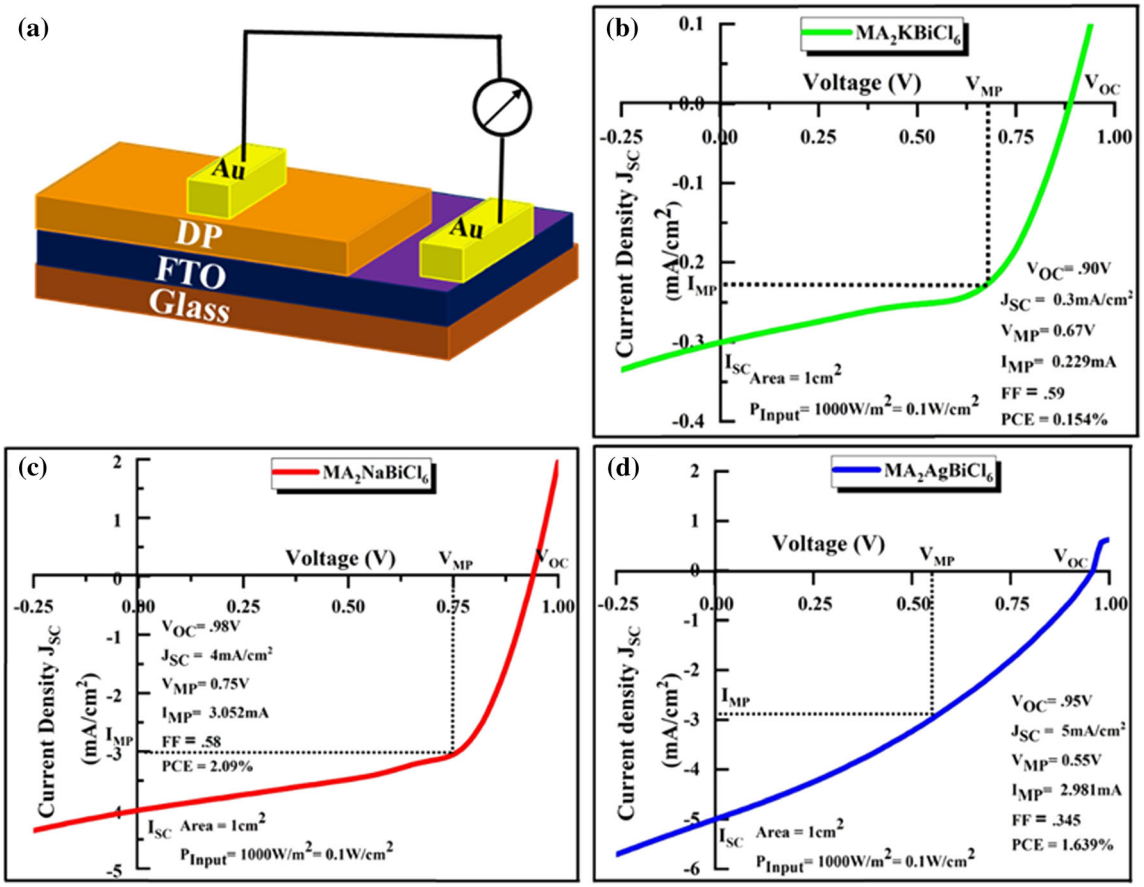


**Figure 9** **a** Schematic diagram of the solar cell device, and illuminated short circuit current density verses voltage characteristic of **a** $MA_2KBiCl_6$ based **b** $MA_2NaBiCl_6$ based, and **c** $MA_2AgBiCl_6$ based device.

**Table 4** Photovoltaic data of the synthesized $MA_2KBiCl_6$, $MA_2NaBiCl_6$ and $MA_2AgBiCl_6$ double perovskite materials

| S. no | Name of the material | $V_{OC}$ (V) | $J_{SC}$ (mA/cm$^2$) | FF (%) | PCE (%) |
|---|---|---|---|---|---|
| 1 | $MA_2KBiCl_6$ | 0.90 | 0.3 | 59 | 0.15 |
| 2 | $MA_2NaBiCl_6$ | 0.98 | 4.0 | 58 | 2.09 |
| 3 | $MA_2AgBiCl_6$ | 0.95 | 5.0 | 34.5 | 1.639 |

showing higher PCE values of 2.09% and 1.679% in comparison with the $MA_2KBiCl_6$-based device having PCE of 0.154%. The possible reason could be the large surface area to volume ratio due to rod like microcrystals structure. Another possible reason could be the high absorption of $MA_2NaBiCl_6$ and $MA_2AgBiCl_6$ in comparison with the $MA_2KBiCl_6$ which can be seen in the absorption profile of these materials. Due to high surface area to volume ratio and high absorption, the light will be absorbed more, which further leads to more electron hole pair generation which increases the reverse current. As the reverse current would increases, leads to high short circuit current density (JSC) and hence PCE will increase resulting a greater short circuit current density of $MA_2NaBiCl_6$ and $MA_2AgBiCl_6$ is greater (4 and 5mA cm$^{-2}$) respectively in comparison with the $J_{SC}$ of $MA_2KBiCl_6$ is 0.3 mA cm$^{-2}$. The device based on $MA_2KBiCl_6$ double perovskite which have vertical flakes morphology leading to low surface area to volume ratio further results into low absorption of light which could be the reason of low PCE as comparison to former two materials.

Further, we have checked the PCE of the all three solar cell devices to check the decay in the PCE as shown in Fig. 11a–c. For this, we have measure the

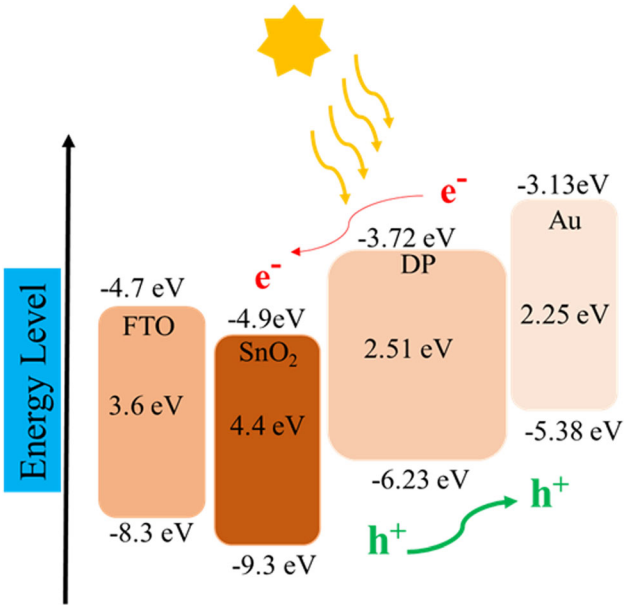


**Figure 10** Illustrating the schematic diagram of energy band diagram of the solar cell device.

PCE of all devices after one week, two week, three week and four week. We have found the PCE decay of 8.9%, 12.1% and 9.9% after one month in $MA_2KBiCl_6$, $MA_2NaBiCl_6$ and $MA_2AgBiCl_6$-based devices, respectively, as shown in Table 5. This is in good agreement with the material stability observed from PL, XRD, and absorption profile of all the samples after a month. The rate of degradation in MA2NaBiCl6 double perovskite material is high as compare to other two double perovskite materials and this behavior can also be seen from PCE data.. In our future work, we will focus on improvement of our perovskite solar cell device functionality in lieu of reduction of PCE with time.

We have performed the experiment of current density–voltage characteristics in forward and reverse bias as well to check the hysteresis at room temperature. We have observed the hysteresis in all three devices. This current density–voltage curve hysteresis in the double perovskites solar cell can be due to the presence of mobile ions [91]. The investigation found that in $MA_2KBiCl_6$-based solar cell having high hysteresis while in $MA_2NaBiCl_6$ and $MA_2AgBiCl_6$-based device having very less current density–voltage hysteresis as shown in Fig. 12a–c. In literature there are evidence that device with high efficiency having low hysteresis while the device with low efficiency will have high hysteresis [88]. In our devices also, it is observed that $MA_2KBiCl_6$-based solar cell having low efficiency in comparison of $MA_2NaBiCl_6$ and $MA_2AgBiCl_6$-based device and therefore $MA_2KBiCl_6$-based solar cell showing high hysteresis. Mainly hysteresis is depends on the diffusion length of charge carriers and on the extent of surface recombination. Ion migration occurs in high-efficiency solar cells but does not result in a high hysteresis effect. Charge extraction in these devices is primarily driven by the diffusion of free electrons and holes [92]. Further, we have calculated the current density of all three devices from external quantum efficiency data also. And we find that the current density calculated from EQE data is almost same as calculated by *I–V* experiment. The calculated current density of $MA_2KBiCl_6$, $MA_2NaBiCl_6$ and $MA_2AgBiCl_6$ from EQE data has shown in Fig. 13a–c.

## Conclusion

For the first time, we have chemically synthesized non-toxic, lead-free, non-degradable hybrid organic–inorganic halide double perovskites $MA_2KBiCl_6$, $MA_2NaBiCl_6$, and $MA_2AgBiCl_6$ material by adopting a novel cost-effective one-step hydrothermal synthesis route. The material characterization was done using various characterization techniques like XRD, PL, FEG-SEM, FTIR, and UV–VIS. The obtained characterization results of XRD have excellent agreement compare to the standard data and showing good crystallinity of the materials. FEG-SEM images of all the synthesized material is having a fine microstructure with vertical micro-flakes and micro-rod kind of structure indicating the possibility of morphology engineering. Our synthesized $MA_2NaBiCl_6$ and $MA_2AgBiCl_6$ DPs are showing rod like structure which is first time reported in the literature. Tolerance and octahedral factor of the synthesized DP NPs are in the required range for the formation of stable 3D structure. Moreover, these materials showed good stability even after one month of exposure of light confirming their non-degradable nature and thus can be used as promising absorber in solar cell applications. In addition, PL and UV–VIS characterization of the synthesized materials shows good photoluminescence and absorbance behavior confirming that the materials are suitable for optical devices. Calculated indirect gaps from Tauc plot of DPs $MA_2KBiCl_6$, $MA_2NaBiCl_6$ and $MA_2AgBiCl_6$ are 2.51 eV, 2.08 eV, and 2.8 eV, respectively, which is

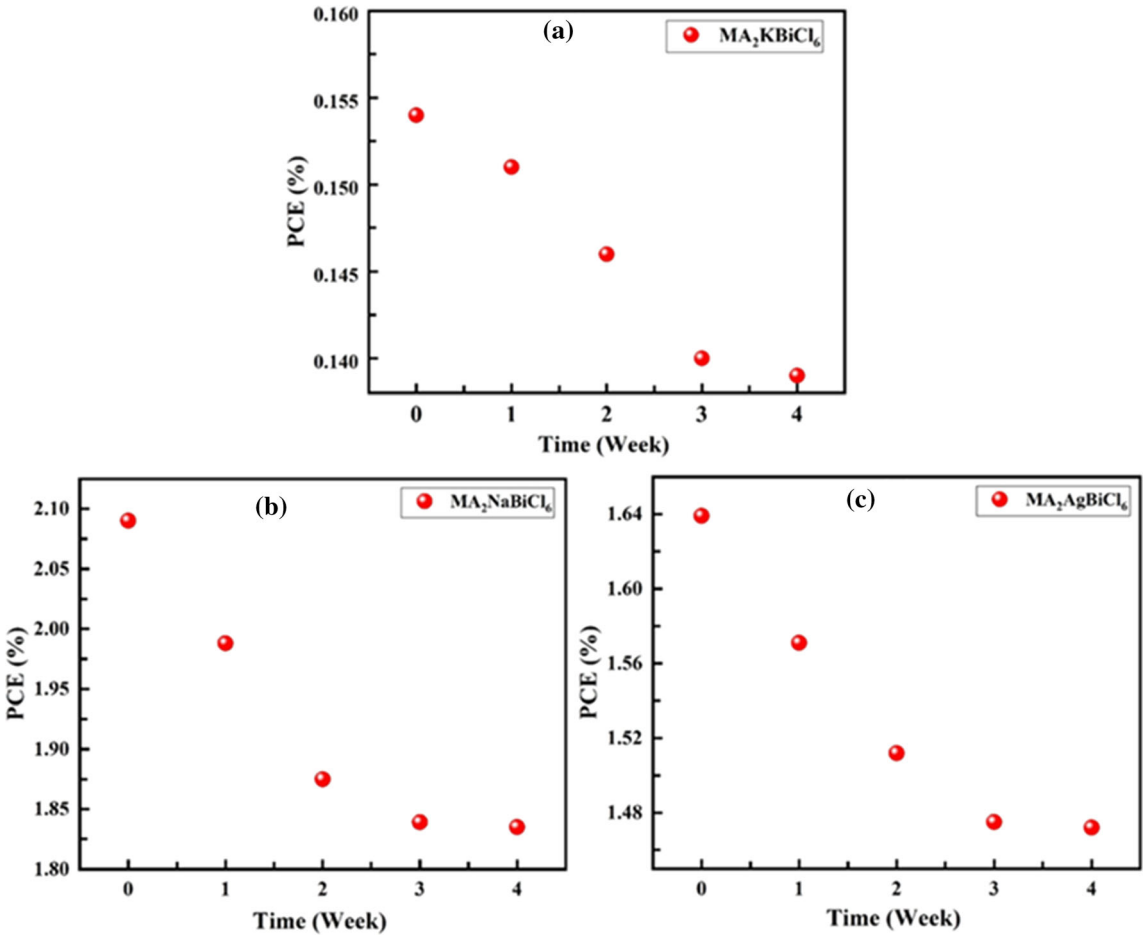


**Figure 11** Illustrating the PCE decay in the device based on **a** MA2KBiCl6, **b** MA2NaBiCl6 and **c** MA2AgBiCl6 after one week, two week, three week and four week.

**Table 5** Photovoltaic data of the synthesized $MA_2KBiCl_6$, $MA_2NaBiCl_6$ and $MA_2AgBiCl_6$ double perovskite materials

| S. no | Name of the material | PCE just after device fabrication (%) | PCE after one week (%) | PCE after two week (%) | PCE after three week (%) | PCE after four week (%) | PCE decay in (%) |
|---|---|---|---|---|---|---|---|
| 1 | $MA_2KBiCl_6$ | 0.154 | 0.151 | 0.146 | 0.14 | 0.139 | 8.9 |
| 2 | $MA_2NaBiCl_6$ | 2.09 | 1.988 | 1.875 | 1.839 | 1.835 | 12.1 |
| 3 | $MA_2AgBiCl_6$ | 1.639 | 1.571 | 1.512 | 1.475 | 1.472 | 9.1 |

suitable band gap for photovoltaic device application. Further we have fabricated all together three solar cell devices and tested the illuminated and dark I-V and calculate PCE of all the three devices. The detected PCE of devices with $MA_2KBiCl_6$, $MA_2NaBiCl_6$ and $MA_2AgBiCl_6$ as absorbing layer was found to be 0.15%, 2.09% and 1.615%, respectively, which is quite remarkable as compare to other reports and its single perovskite counterpart. The solar cell device based on $MA_2NaBiCl_6$ DP showed the best performance as compare to other two devices. In conclusion, the overall material characterization and fabricated devices result shows that these double perovskites materials are promising replacements of the single perovskite in every aspects for photovoltaic utility. Our present work shows that other possible stable and high performing inorganic and organic–inorganic halide-based double perovskites should be explored for optoelectronic and photovoltaic utility. Our future efforts will involve in

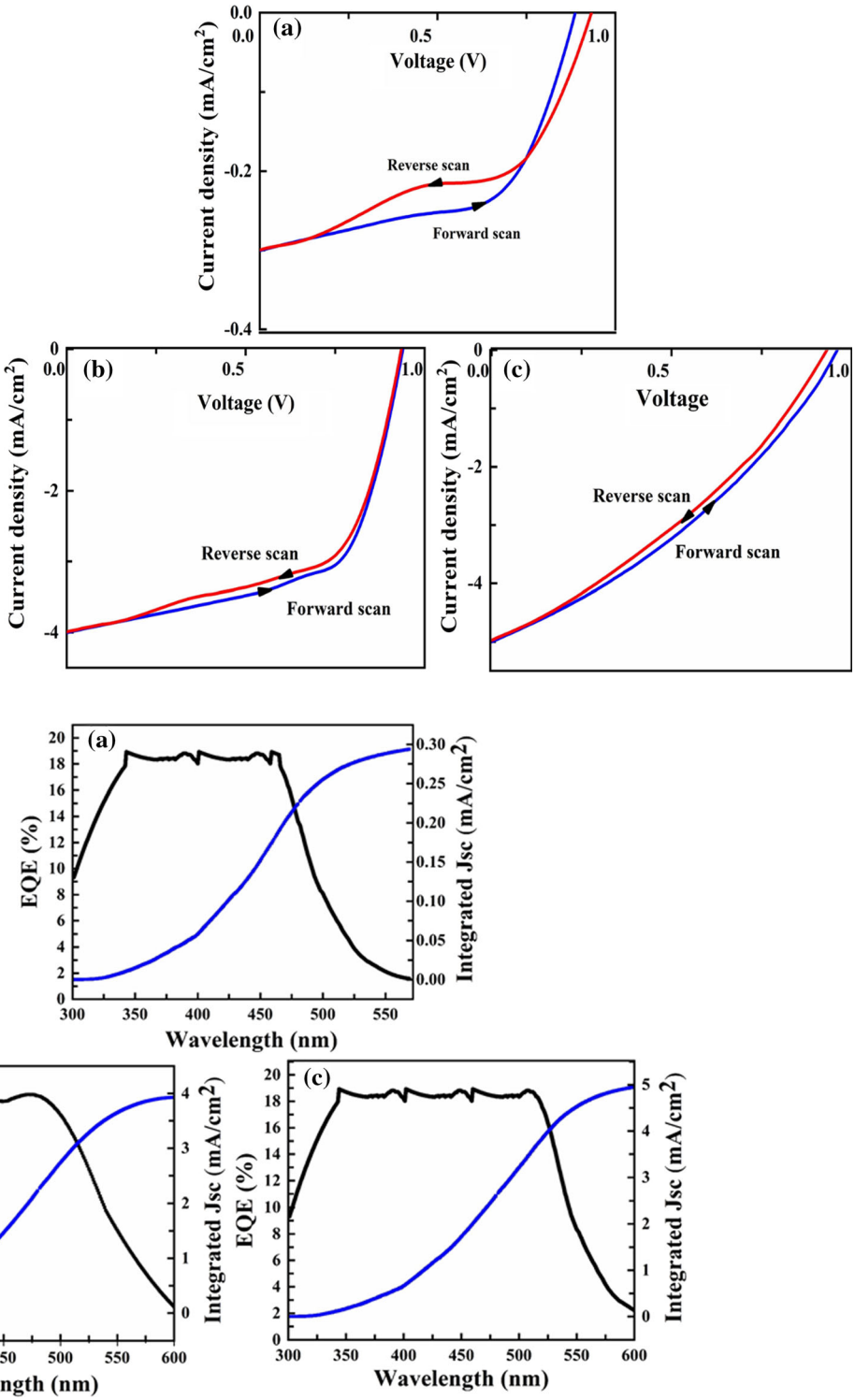


**Figure 12** Observed hysteresis in forward and reverse scan of current density–voltage **a** MA2KBiCl6 **b** MA2NaBiCl6, and **c** MA2AgBiCl6.

**Figure 13** Current density calculated from EQE in **a** $MA_2KBiCl_6$ **b** $MA_2NaBiCl_6$, and **c** $MA_2AgBiCl_6$.

experimental realization of various double perovskites as a greener alternative to single perovskite for application in various domains.

## Acknowledgements

The authors would like to thank the following funding sources that supported the research presented. 1. Sophisticated Analytical Instrument Facility (SAIF) at IIT Bombay for providing a characterization facility. 2. The Prime Minister Research Fellowship (PMRF) under Ministry of education (MOE) for research grant provide to Neelu. (PMRF-1301164 is PMRF ID under which research grant is provided). 3. The Indian Institute of Technology (IIT) Bombay, Mumbai, India for providing the Institute Post-Doctoral Fellow (IPDF) position to Nivedita Pandey.

## Author contribution

NN contributed to conceptualization, investigation, writing—original draft preparation, writing—review and editing. NP contributed to conceptualization, investigation, writing—original draft preparation, writing—review and editing. SC contributed to supervision, writing—reviewing and editing.

## Data and code availability

Due to the sensitive nature of the data, information created during and/or analyzed during the current study is available from the corresponding author on reasonable request to bona fide researchers.

## Declarations

**Conflict of interest** The authors declare that they have no known competing financial interests or personal relationships that could have appeared to influence the work reported in this paper.

**Ethical approval** We the undersigned declare that this manuscript is original, has not been published before and is not currently being considered for publication elsewhere. We confirm that the manuscript has been read and approved by all named authors and that there are no other persons who satisfied the criteria for authorship but are not listed. We further confirm that the order of authors listed in the manuscript has been approved by all of us. We understand that the Corresponding Author is the sole contact for the Editorial process. He/she is responsible for communicating with the other authors about progress, submissions of revisions and final approval of proofs.

## References

[1] Xing G, Mathews N, Sun S, Lim SS, Lam YM, Grätzel M, Sum TC (2013) Long-range balanced electron-and hole-transport lengths in organic-inorganic $CH_3NH_3PbI_3$. Science 342:344–347

[2] Giorgi G, Fujisawa JI, Segawa H, Yamashita K (2013) Small photocarrier effective masses featuring ambipolar transport in methylammonium lead iodide perovskite: a density functional analysis. J Phys Chem Lett 4:4213–4216

[3] Frohna K, Deshpande T, Harter J, Peng W, Barker BA, Neaton JB, Bernardi M (2018) Inversion symmetry and bulk Rashba effect in methylammonium lead iodide perovskite single crystals. Nat Commun 9:1829

[4] Stranks SD, Eperon GE, Grancini G, Menelaou C, Alcocer MJ, Leijtens T, Snaith HJ (2013) Electron-hole diffusion lengths exceeding 1 micrometer in an organometal trihalide perovskite absorber. Science 342:341–344

[5] Wehrenfennig C, Eperon GE, Johnston MB, Snaith HJ, Herz LM (2014) High charge carrier mobilities and lifetimes in organolead trihalide perovskites. Adv Mater 26:1584–1589

[6] Edri E, Kirmayer S, Mukhopadhyay S, Gartsman K, Hodes G, Cahen D (2014) Elucidating the charge carrier separation and working mechanism of $CH_3NH_3PbI_3-$ x Cl x perovskite solar cells. Nat Commun 5:3461

[7] Miyata A, Mitioglu A, Plochocka P, Portugall O, Wang JTW, Stranks SD, Nicholas RJ (2015) Direct measurement of the exciton binding energy and effective masses for charge carriers in organic–inorganic tri-halide perovskites. Nat Phys 11:582–587

[8] Baumann A, Väth S, Rieder P, Heiber MC, Tvingstedt K, Dyakonov V (2015) Identification of trap states in perovskite solar cells. J Phys Chem Lett 6:2350–2354

[9] Duan HS, Zhou H, Chen Q, Sun P, Luo S, Song TB, Yang Y (2015) The identification and characterization of defect states in hybrid organic–inorganic perovskite photovoltaics. Phys Chem Chem Phys 17:112–116

[10] Wang JTW, Wang Z, Pathak S, Zhang W, deQuilettes DW, Wisnivesky-Rocca-Rivarola F, Snaith HJ (2016) Efficient

perovskite solar cells by metal ion doping. Energy Environ Sci 9:2892–2901

[11] Zhao D, Yu Y, Wang C, Liao W, Shrestha N, Grice CR, Yan Y (2017) Low-bandgap mixed tin–lead iodide perovskite absorbers with long carrier lifetimes for all-perovskite tandem solar cells. Nat Energy 2:1–7

[12] Pandey N, Kumar A, Chakrabarti S (2019) Investigation of the structural, electronic, and optical properties of Mn-doped $CsPbCl_3$: theory and experiment. RSC Adv 9:29556–29565

[13] Pandey N, Chakrabarti S (2020) Understanding the effect of Mn doping in $CsPbBr_3$ using ab-initio method with experimental validation. IEEE J Photovolt 10:1359–1364

[14] Pandey N, Chakrabarti S (2021) Tuning the morphological, photophysical, and electronic properties of CsPb $(Cl/Br)_3$ by impurity doping for optoelectronic applications: a theoretical and experimental study. IEEE J Photovolt 11:379–385

[15] Pandey N, Chakrabarti S (2022) Ab initio computational details with facile high-temperature synthesis of pure and alloyed $CsPbI_3$ with inherent stability analysis for optoelectronic applications. IEEE J Photovolt 12:625–633

[16] Kojima A, Teshima K, Shirai Y, Miyasaka T (2009) Organometal halide perovskites as visible-light sensitizers for photovoltaic cells. J Am Chem Soc 131:6050–6051

[17] Kim HS, Lee CR, Im JH, Lee KB, Moehl T, Marchioro A, Park NG (2012) Lead iodide perovskite sensitized all-solid-state submicron thin film mesoscopic solar cell with efficiency exceeding 9%. Sci Rep 2:591

[18] Saliba M, Matsui T, Domanski K, Seo JY, Ummadisingu A, Zakeeruddin SM, Grätzel M (2016) Incorporation of rubidium cations into perovskite solar cells improves photovoltaic performance. Science 354:206–209

[19] Saliba M, Matsui T, Seo JY, Domanski K, Correa-Baena JP, Nazeeruddin MK, Grätzel M (2016) Cesium-containing triple cation perovskite solar cells: improved stability, reproducibility and high efficiency. Energy Environ Sci 9:1989–1997

[20] McMeekin DP, Sadoughi G, Rehman W, Eperon GE, Saliba M, Hörantner MT, Snaith HJ (2016) A mixed-cation lead mixed-halide perovskite absorber for tandem solar cells. Science 351:151–155

[21] Shao Y, Yuan Y, Huang J (2016) Correlation of energy disorder and open-circuit voltage in hybrid perovskite solar cells. Nat Energy 1:1–6

[22] Yang WS, Park BW, Jung EH, Jeon NJ, Kim YC, Lee DU, Seok SI (2017) Iodide management in formamidinium-lead-halide–based perovskite layers for efficient solar cells. Science 356:1376–1379

[23] D'innocenzo V, Grancini G, Alcocer MJ, Kandada ARS, Stranks SD, Lee M, Petrozza A (2014) Excitons versus free charges in organo-lead tri-halide perovskites. Nat Commun 5:3586

[24] Burschka J, Pellet N, Moon SJ, Humphry-Baker R, Gao P, Nazeeruddin MK, Grätzel M (2013) Sequential deposition as a route to high-performance perovskite-sensitized solar cells. Nature 499:316–319

[25] Liu M, Johnston MB, Snaith HJ (2013) Efficient planar heterojunction perovskite solar cells by vapour deposition. Nature 501:395–398

[26] Zhou H, Chen Q, Li G, Luo S, Song TB, Duan HS, Yang Y (2014) Interface engineering of highly efficient perovskite solar cells. Science 345:542–546

[27] Jeon NJ, Noh JH, Kim YC, Yang WS, Ryu S, Seok SI (2014) Solvent engineering for high-performance inorganic–organic hybrid perovskite solar cells. Nat Mater 13:897–903

[28] Jeon NJ, Noh JH, Yang WS, Kim YC, Ryu S, Seo J, Seok SI (2015) Compositional engineering of perovskite materials for high-performance solar cells. Nature 517:476–480

[29] Yang WS, Noh JH, Jeon NJ, Kim YC, Ryu S, Seo J, Seok SI (2015) High-performance photovoltaic perovskite layers fabricated through intramolecular exchange. Science 348:1234–1237

[30] Chen W, Wu Y, Yue Y, Liu J, Zhang W, Yang X, Han L (2015) Efficient and stable large-area perovskite solar cells with inorganic charge extraction layers. Science 350:944–948

[31] National Renewable Energy Laboratory (NREL) (2018) https://www.nrel.gov/pv/assets/pdfs/pv-efciencies-chart.20181

[32] Gao D, Bo L, Zhen L, Xin W, Shoufeng Z, Dan Z, Xiaofen J (2023) Highly efficient flexible perovskite solar cells through pentylammonium acetate modification with certified efficiency of 23.35%. Adv Mater 3: 2206387

[33] Hui W, Xinxin K, Baohua W, Deli L, Zhenhuang S, Yaqi B, Lei G (2023) Stable electron-transport-layer-free perovskite solar cells with over 22% power conversion efficiency. Nano Lett 6:2195–2202

[34] Chen Z, Li H, Tang Y, Huang X, Ho D, Lee CS (2014) Shape-controlled synthesis of organolead halide perovskite nanocrystals and their tunable optical absorption. Mater Res Express 1:015034

[35] Stranks SD, Snaith HJ (2015) Metal-halide perovskites for photovoltaic and light-emitting devices. Nat Nanotechnol 10:391–402

[36] Cho H, Jeong SH, Park MH, Kim YH, Wolf C, Lee CL, Lee TW (2015) Overcoming the electroluminescence efficiency limitations of perovskite light-emitting diodes. Science 350:1222–1225

[37] Chen Q, Wu J, Ou X, Huang B, Almutlaq J, Zhumekenov AA, Liu X (2018) All-inorganic perovskite nanocrystal scintillators. Nature 561:88–93

[38] Zhang F, Yang B, Zheng K, Yang S, Li Y, Den W, He R (2018) Formamidinium lead bromide ($FAPbBr_3$) perovskite microcrystals for sensitive and fast photodetectors. Nano-Micro Lett 10:1–8

[39] Chu L, Hu R, Liu W, Ma Y, Zhang R, Yang J, Li XA (2018) Screen printing large-area organometal halide perovskite thin films for efficient photodetectors. Mater Res Bull 98:322–327

[40] Qin X, Zhao Z, Wang Y, Wu J, Jiang Q, You J (2017) Recent progress in stability of perovskite solar cells. J Semicond 38:011002

[41] Xiao Z, Meng W, Wang J, Mitzi DB, Yan Y (2017) Searching for promising new perovskite-based photovoltaic absorbers: the importance of electronic dimensionality. Mater Horiz 4:206–216

[42] Zhang Q, Ting H, Wei S, Huang D, Wu C, Sun W, Xiao L (2018) Recent progress in lead-free perovskite (-like) solar cells. Mater Today Energy 8:157–165

[43] Nasti G, Abate A (2020) Tin halide perovskite (ASnX3) solar cells: a comprehensive guide toward the highest power conversion efficiency. Adv Energy Mater 10:1902467

[44] Liang L, Gao P (2018) Lead-free hybrid perovskite absorbers for viable application: can we eat the cake and have it too? Adv Sci 5:1700331

[45] Abate A (2017) Perovskite solar cells go lead free. Joule 1:659–664

[46] Yin WJ, Shi T, Yan Y (2014) Unique properties of halide perovskites as possible origins of the superior solar cell performance. Adv Mater 26:4653–4658

[47] Zhao XG, Yang D, Ren JC, Sun Y, Xiao Z, Zhang L (2018) Rational design of halide double perovskites for optoelectronic applications. Joule 2:1662–1673

[48] Todd S (2018) Pump probe studies of spin dynamics in the 2D perovskite butylammonium methylammonium lead iodide

[49] Ghosh B, Chakraborty S, Wei H, Guet C, Li S, Mhaisalkar S, Mathews N (2017) Poor photovoltaic performance of $Cs_3Bi_2I_9$: an insight through first-principles calculations. J Phys Chem C 121:17062–17067

[50] Zhao XG, Yang JH, Fu Y, Yang D, Xu Q, Yu L, Zhang L (2017) Design of lead-free inorganic halide perovskites for solar cells via cation-transmutation. J Am Chem Soc 139:2630–2638

[51] Bai T, Yang B, Chen J, Zheng D, Tang Z, Wang X, Han K (2021) Efficient luminescent halide quadruple-perovskite nanocrystals via trap-engineering for highly sensitive photodetectors. Adv Mater 33:2007215

[52] Hoseinpour V, Zahra S, Luis E (2023) Design, synthesis, optical studies, and application of all-inorganic layered double perovskites as stabilizers in ambient air processed perovskite solar cells. Mater Res Bull 159:112088

[53] Pandey N, Neelu N, Chakrabarti S (2023) Room temperature synthesis of double perovskite $Cs_2AlBiCl_6$ for photovoltaic applications. Opt Mater 137:113570

[54] Li B, Xin W, Shoufeng Z, Zhen L, Danpeng G, Xiankai C, Shuang X, Chu-Chen C, Alex KYJ, Zonglong Z (2022) Efficient and stable $Cs_2AgBiBr_6$ double perovskite solar cells through in-situ surface modulation. Chem Eng J 446:137144

[55] Li, J, Xianghuan M, Zhiheng W, Yanyan D, Ruxin , Weidong X, Yongshang Z (2022) Pinning bromide ion with ionic liquid in lead-free $Cs_2AgBiBr_6$ double perovskite solar cells. Adv Funct Mater 32:2112991

[56] Tang, CW (1986) Two-layer organic photovoltaic cell. Appl Phys Lett 48:183–185

[57] Krebs Frederik C (2009) Fabrication and processing of polymer solar cells: A review of printing and coating techniques. Solar Energy Mater Solar Cells 93:394–412

[58] Zhokhavet U, Tobias E, Gerhard G, Maher A, Oliver A (2006) Relation between absorption and crystallinity of poly (3-hexylthiophene)/fullerene films for plastic solar cells. Chem Phys Lett 418:347–350

[59] Zhou Y, Michael E, Michael K (2010) Bulk-heterojunction hybrid solar cells based on colloidal nanocrystals and conjugated polymers. Energy Environ Sci 12:1851–1864

[60] Zhou Y, Michael E, Clemens V, Birger Z, Frank R, Phenwisa N, Seyfullah Y (2011) Efficiency enhancement for bulk-heterojunction hybrid solar cells based on acid treated CdSe quantum dots and low bandgap polymer PCPDTBT. Sol Energy Mater Sol Cells 4:1232–1237

[61] Dayal S, Kopidakis N, Olson DC, Ginley DS, Rumbles G (2010) Photovoltaic devices with a low band gap polymer and CdSe nanostructures exceeding 3% efficiency. Nano Lett 1:239–242

[62] Nath A, Bhati N, Mahajan BK, Rakshit JK, Sarkar MB (2022) Silver nanoparticles textured oxide thin films for surface plasmon enhanced photovoltaic properties. Plasmonics 1:193–201

[63] Zhao XG, Yang D, Sun Y, Li T, Zhang L, Yu L, Zunger A (2017) Cu–In halide perovskite solar absorbers. J Am Chem Soc 139:6718–6725

[64] Wei F, Deng Z, Sun S, Xie F, Kieslich G, Evans DM, Cheetham AK (2016) The synthesis, structure and electronic properties of a lead-free hybrid inorganic–organic double perovskite (MA) 2 $KBiCl_6$ (MA= methylammonium). Mater Horiz 3:328–332

[65] Fatimah S, Ragadhita R, Al Husaeni DF, Nandiyanto ABD (2022) How to calculate crystallite size from x-ray diffraction (XRD) using Scherrer method. ASEAN J Sci Eng 2:65–76

[66] Schmitz F, Horn J, Dengo N, Sedykh AE, Becker J, Maiworm E, Gatti T (2021) Large cation engineering in two-dimensional silver–bismuth bromide double perovskites. Chem Mater 33:4688–4700

[67] Mir SA, Gupta DC (2021) Analysis of cage structured halide double perovskites Cs2NaMCl6 (M= Ti, V) by spin polarized calculations. J Alloy Compd 854:156000

[68] Pering SR, Deng W, Troughton JR, Kubiak PS, Ghosh D, Niemann RG, Cameron PJ (2017) Azetidinium lead iodide for perovskite solar cells. J Mater Chem A 5:20658–20665

[69] Boix PP, Agarwala S, Koh TM, Mathews N, Mhaisalkar SG (2015) Perovskite solar cells: beyond methylammonium lead iodide. J Phys Chem Lett 6:898–907

[70] Dimesso L, Wussler M, Mayer T, Mankel E, Jaegermann W (2016) Inorganic alkali lead iodide semiconducting $APbI_3$ (A= Li, Na, K, Cs) and $NH_4PbI_3$ films prepared from solution: structure, morphology, and electronic structure. AIMS Mater Sci 3:737–755

[71] Li H, Sadler PJ, Sun H (1996) Unexpectedly strong binding of a large metal ion ($Bi^{3+}$) to human serum transferrin (∗). J Biol Chem 271:9483–9489

[72] Thind AS, Kavadiya S, Kouhnavard M, Wheelus R, Cho SB, Lin LY, Mishra R (2019) $KBaTeBiO_6$: a lead-free, inorganic double-perovskite semiconductor for photovoltaic applications. Chem Mater 31:4769–4778

[73] Yangui A, Garrot D, Lauret JS, Lusson A, Bouchez G, Deleporte E, Boukheddaden K (2015) Optical investigation of broadband white-light emission in self-assembled organic–inorganic perovskite $(C_6H_{11}NH_3)$ $2PbBr_4$. J Phys Chem C 119:23638–23647

[74] McCall KM, Stoumpos CC, Kostina SS, Kanatzidis MG, Wessels BW (2017) Strong electron–phonon coupling and self-trapped excitons in the defect halide perovskites A3M2I9 (A= Cs, Rb; M= Bi, Sb). Chem Mater 29:4129–4145

[75] Jeon IK, Abdullah A, Hussein AJ, Yong-Rak K, Ashrant A, Juan-Carlos B (2023) Effects of shape-stabilized phase change materials in cementitious composites on thermal-mechanical properties and economic benefits. Appl Therm Eng 219:119444

[76] Ghasemi M, Mengmeng H, Mu X, Peng C, Dongxu H, Yurou Z, Weijian C (2020) Lead-free metal-halide double perovskites: from optoelectronic properties to applications. Nanophotonics 8:2181–2219

[77] Wei F, Zeyu D, Shijing S, Fenghua Z, Donald M. E, Gregor K, Satoshi T (2017) Synthesis and properties of a lead-free hybrid double perovskite:$(CH_3NH_3)$ $2AgBiBr_6$. Chem Mater 3:1089–1094

[78] McClure ET, Molly RB, Wolfgang W, Patrick MW (2016) $Cs_2AgBiX_6$ (X= Br, Cl): new visible light absorbing, lead-free halide perovskite semiconductors. Chem Mater 5:1348–1354

[79] Volonakis G, Filip MR, Haghighirad AA, Sakai N, Wenger B, Snaith, HJ, Giustino F (2016) Lead-free halide double perovskites via heterovalent substitution of noble metals. J Phys Chem Lett

[80] Slavney AH, Hu T, Lindenberg AM, Karunadasa HI (2016) A bismuth-halide double perovskite with long carrier recombination lifetime for photovoltaic applications. J Am Chem Soc 7:2138–2141

[81] Popple D, Mehmet D, Tony VH, Scott S, Peter E, Karen CB, Marvin C, Alex Z (2023) Charge-induced phase transition in encapsulated Hf $Te_2$ nanoribbons. Phys Rev Mater 1:L013001

[82] Li L, Shao H, Wu X, Chen W, Zhu J, Dong B, Bai X (2022) Aluminum-doped lead-free double perovskite $Cs_2AgBiCl_6$ nanocrystals with ultrahigh stability towards white light emitting diodes. Mater Res Bull 147:111645

[83] Liu Z, Yang H, Wang J, Yuan Y, Hills-Kimball K, Cai T, Chen O (2021) Synthesis of lead-free $Cs_2AgBiX_6$ (X= Cl, Br, I) double perovskite nanoplatelets and their application in $CO_2$ photocatalytic reduction. Nano Lett 21:1620–1627

[84] Lu M, Zhang X, Bai X, Wu H, Shen X, Zhang Y, Rogach AL (2018) Spontaneous silver doping and surface passivation of $CsPbI_3$ perovskite active layer enable light-emitting devices with an external quantum efficiency of 11.2%. ACS Energy Lett 3:1571–1577

[85] Wang KQ, He Y, Zhang M, Shi JJ, Cai WW (2021) Promising lead-free double-perovskite photovoltaic materials Cs2MM′ Br 6 (M= Cu, Ag, and Au; M′= Ga, In, Sb, and Bi) with an ideal band gap and high power conversion efficiency. J Phys Chem C 125:21160–21168

[86] Lingegowda DC, Kumar JK, Prasad AD, Zarei M, Gopal S (2012) FTIR spectroscopic studies on Cleome gynandra–comparative analysis of functional group before and after extraction. Rom J Biophys 22:137–143

[87] Salem Marwa S, Mostafa MS, Mohamed MA, Ahmed S, Abdullah JA, Adwan A, Rabie R (2021) Efficient perovskite solar cell without electron transport layer. Int J Electr Eng Technol 34(12):1

[88] Sun H, Yu Z, Yu X, Kaimo D, Linxing M, Jie X, Liang L (2019) Composition and energy band-modified commercial FTO substrate for in situ formed highly efficient electron transport layer in planar perovskite solar cells. Adv Funct Mater 11:1808667

[89] Shalan AE, Tomoya O, Sudhakar N, Mahmoud ME, Kosei U, Hui-Ping W, Keisuke N, Xu S, Eric Wei-Guang D, Hiroaki M (2016) Cobalt oxide (CoOx) as an efficient hole-extracting layer for high-performance inverted planar perovskite solar cells. ACS Appl Mater Interfaces 49:33592–33600

[90] Hussain I, Hoang Phong T, Jared J, Justin M, Nazmul I, Jasim M U (2018) Functional materials, device architecture, and flexibility of perovskite solar cell. Emerg Mater 1:133–154

[91] Ren J, Kan Z (2020) Chapter 1: origin of hysteresis in perovskite solar cells. AIP Publishing LLC, Melville

[92] Neukom MT, Züfle S, Knapp E, Makha M, Hany R, Ruhstaller B (2017) Why perovskite solar cells with high efficiency show small IV-curve hysteresis. Sol Energy Mater Sol Cells 169:159–166